Proceedings of the
Annual Stability Conference
Structural Stability Research Council
Grapevine, Texas, April 18-21, 2012

GBT-Based Assessment of the Buckling Behavior of Cold-Formed Steel Purlins Restrained by Sheeting

A. Graça[1], C. Basaglia[1], D. Camotim[1], R. Gonçalves[2]

Abstract

This work presents and discusses the results of a GBT-based numerical investigation concerning the local, distortional and global buckling behavior of lipped channel and zed-section cold-formed steel purlins restrained by steel sheeting and subjected to an uplift loading. Strengthened (lapped) joints, commonly employed at internal supports to preclude the occurrence of local/distortional buckling phenomena, are also investigated and a strategy to determine "optimal strengthening lengths" is devised. The sheeting restraint is modeled by means of elastic translational and rotational springs, located at the purlin upper flange, and the joint strengthening is modeled by doubling the cross-section wall thickness. For validation, the GBT-based results are compared with ANSYS shell finite element model values.

1. Introduction

The last two decades have witnessed a significant reduction in the use of heavy sheeting in industrial buildings (*e.g.*, fiber cement roof sheets), as they have been increasingly replaced by lighter sheeting, such as cold-formed steel sheeting, which is more cost-efficient and easier/quicker to construct/erect (*e.g.*, Davies 1991). This is because the hook bolts, previously used to connect the roof sheeting to the cold-formed steel purlins, have been gradually replaced by self-drilling screws, which lead to a higher structural efficiency of the purlin-sheeting assembly (*e.g.*, Freitas 2004). Thus, it is economically advantageous (and makes full structural sense) to base the purlin design on the joint behavior of the whole purlin-sheeting assembly, instead of adopting the traditional approach of viewing the purlins as independent/isolated members. For instance, in the case of purlins subjected to uplift loading, the sheeting restraint changes the buckling mode nature from lateral-torsional to lateral-distortional, as shown in Fig. 1.

The structural efficiency of open-section thin-walled steel purlins connected to roof sheeting and acted by wind uplift can only be adequately assessed after acquiring in-depth information on the mechanics of its buckling behavior, a task involving (i) the identification of the relevant buckling modes and (ii) the calculation of the associated critical buckling (bifurcation) stresses. However, since these purlins (i) are partially restrained by the roof sheeting, both laterally and torsionally, (ii) display very slender cross-sections, making them highly susceptible to local, distortional and global instability phenomena,

[1] ICIST, Instituto Superior Técnico, Technical University of Lisbon, Portugal.
<andre.biscaya@gmail.com>, <cilmarbasaglia@gmail.com>, <dcamotim@civil.ist.utl.pt>
[2] UNIC, Faculdade de Ciências e Tecnolgia, Universidade Nova de Lisboa, Portugal.
<rodrigo.goncalves@fct.unl.pt>

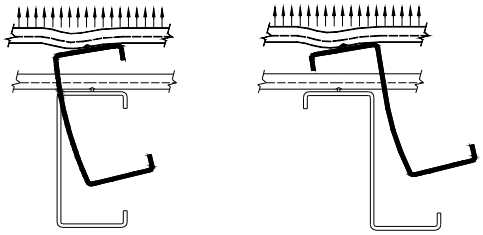

Figure 1: Lateral-distortional buckling mode configuration of lipped channel and zed-section purlins restrained by roof sheeting and subjected to an uplift uniformly distributed load.

and (iii) often exhibit lapped (strengthened) joints over the internal supports, the assessment of their structural response constitutes a very complex task, requiring the performance of either (i) costly and carefully planned experimental test programs or (ii) complex and time-consuming (including data input and result interpretation) shell finite element analyses. A very promising alternative is the use of one-dimensional models (beam finite elements) based on Generalized Beam Theory (GBT), a beam theory incorporating genuine folded-plate concepts (*e.g.*, Silvestre & Camotim 2002a,b or Camotim *et al.* 2004). In particular, GBT-based beam finite elements can accurately assess the local, distortional and global buckling behavior of thin-walled single and multi-span beams, handling both arbitrary loadings and localized flange displacement and/or rotation restraints in cross-sections located along the beam length – such restraints are modeled as elastic translational and/or rotational springs (Camotim *et al.* 2008, 2010).

The aim of this work is to present and discuss the results of a numerical (GBT-based) investigation concerning the local, distortional and global buckling behavior of lipped channel and zed-section cold-formed steel purlins (i) restrained by steel sheeting and (ii) subjected to uplift distributed loads. Particular attention is devoted to assessing (i) how the restraints provided by the sheeting influence the buckling behavior of single and multi-span purlins, and also (ii) what is the minimum joint strengthening (lapped) length required to preclude the occurrence of local buckling effects near multi-span beam intermediate supports, thus making it possible to suppress the purlin vulnerability in this zone with the least added material. The sheeting restraint is simulated by means of elastic translational and rotational supports (springs) located at the purlin upper flange mid-width. The joint strengthening is modeled by doubling the purlin wall thickness along the whole lapped length, while assuming full continuity. The numerical results presented and discussed are obtained through (i) GBT-based beam finite element analyses and, for validation/comparison purposes, also by means of (ii) ANSYS (SAS 2009) shell finite element analyses.

2. GBT-Based Beam Finite Element Formulation for Purlin/Sheeting Systems

The performance of a GBT-based structural analysis involves two main tasks, namely (i) a *cross-section analysis*, aimed at identifying the deformation modes and evaluating the associated modal mechanical properties, and (ii) a *member analysis* (first order, buckling, vibration, etc.), involving the solution of the appropriate differential equilibrium equations and the interpretation of the (modal) results obtained. In order to incorporate elastic restraints in a GBT buckling analysis, two main approaches can be followed. In the first one, which is only valid for members uniformly restrained along their axes, the restraints are incorporated into the cross-section analysis, *i.e.*, are taken into account when calculating the cross-section deformation modes (Schardt 1989, Davies *et al*. 1994). In the second approach, which is more general and allows handling members continuously and discretely restrained along their axes, the elastic restraints are included in the member analysis as constraint equations, *i.e.*, the deformation modes are calculated without restraints (Camotim *et al.* 2008). Moreover, retaining the "classical" cross-section deformation

modes (axial extension, bending, torsion, distortion, etc.) contributes to a clearer structural interpretation of the results – this fact played a key role in opting for the second approach in this work.

Consider the prismatic thin-walled member with arbitrary open cross-section depicted in Fig. 2, where x, s and z are local coordinates along the member axis, cross-section mid-line and wall thickness, thus leading to member mid-surface displacement components $u(x,s)$, $v(x,s)$ and $w(x,s)$ expressed by

$$u(x,s) = u_k(s)\phi_{k,x}(x) \qquad v(x,s) = v_k(s)\phi_k(x) \qquad w(x,s) = w_k(s)\phi_k(x) \quad , \quad (1)$$

where (i) $(.)_{,x} \equiv d(.)/dx$, (ii) the summation convention applies to subscript k, (iii) functions $u_k(s)$, $v_k(s)$, $w_k(s)$ are displacement components of deformation mode k, obtained from the GBT cross-section analysis, and (iv) $\phi_k(x)$ are mode amplitude functions defined along the member length.

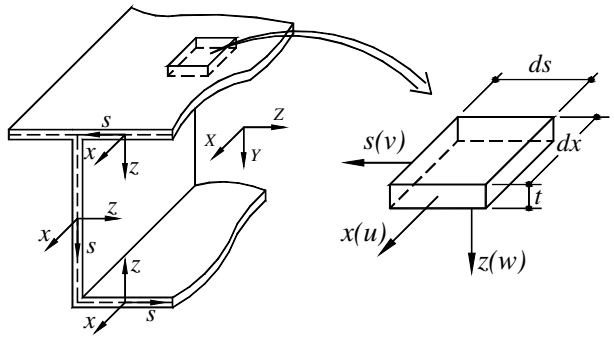

Figure 2: Prismatic thin-walled member with an arbitrary open cross-section and local coordinate axes.

2.1 Total potential energy

The member equilibrium equations including the elastic constraints (springs) are obtained from the variational condition

$$\delta V = \delta U + \delta U_S + \delta\Pi_{\sigma-x} + \delta\Pi_\tau = \int_\Omega \sigma_{ij}\delta\varepsilon_{ij}d\Omega + \int_L \kappa\delta\Delta_R dx + \sum_{P=1}^{m} K\Delta_P + \int_\Omega \sigma^0_{xx}\delta\varepsilon_{xx}d\Omega + \int_\Omega \tau^0_{xs}\delta\gamma_{xs}d\Omega = 0 \quad , \quad (2)$$

where (i) Ω is the structural system volume (n plates), (ii) L is the member length, (iii) δU is the first variation of the strain energy, given by the tensor product between the internal stresses σ_{ij} ($\sigma_{xs} \equiv \tau_{xs}$) and the strain variations $\delta\varepsilon_{ij}$ ($\delta\varepsilon_{xs} \equiv \delta\gamma_{xs}$) associated with the buckling action/mode, (iv) δU_S is the first variation of the potential energy of continuous and discrete springs with stiffness κ and K (distributed along the longitudinal axis R and located at points P, respectively), (v) Δ is the spring generalized displacement, and (vi) $\delta\Pi_{\sigma-x}$ and $\delta\Pi_\tau$ are the works done by the pre-buckling longitudinal normal (σ^0_{xx}) and shear (τ^0_{xs}) stresses, deemed constant with their final values and statically equivalent to the (longitudinally varying) internal forces, moments and bimoments, over the strain variations $\delta\varepsilon_{ij}$.

In this work, the modeling of the restraint provided by the sheeting to the purlin comprises continuous or discrete translational and rotational springs with stiffness k_y and k_θ (continuous) or K_y and K_θ (discrete), which provide restraint against (i) the horizontal displacements (along Y) and (ii) mid-width rotations (about X) of the purlin upper flange – Fig. 3 illustrates the case of discrete springs, where a is the longitudinal spacing between consecutive restraints (*i.e.*, between the points where the sheeting/purlin joints are deemed materialized).

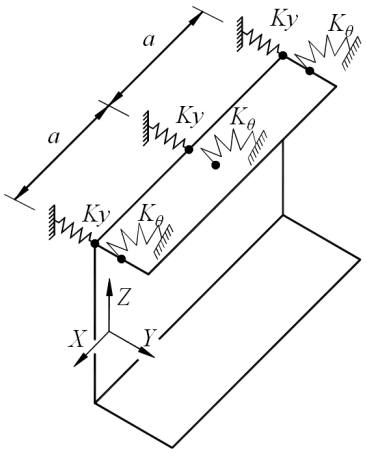

Figure 3: Discrete elastic springs spaced by a.

Then, the variational form of the equilibrium conditions reads

$$\delta V = \int_L \Big(C_{ik}\phi_{k,xx}\delta\phi_{i,xx} + D^1_{ik}\phi_{k,x}\delta\phi_{i,x} + D^2_{ik}\phi_k\delta\phi_{i,xx} + D^2_{ki}\phi_{k,xx}\delta\phi_i + B_{ik}\phi_k\delta\phi_i + \\ + f^y_{R.ik}\phi_k\delta\phi_i + f^\theta_{R.ik}\phi_k\delta\phi_i \Big)dx + \sum_{P=1}^{m} F^y_{P.ik}\phi_k(x_P)\delta\phi_i(x_P) + \sum_{P=1}^{m} F^\theta_{P.ik}\phi_k(x_P)\delta\phi_i(x_P) + \\ + \lambda\int_L \Big([W^0_j X^{\sigma-x}_{jik}\phi_{k,x}\delta\phi_{i,x} - W^0_{j,x} X^\tau_{jik}(\phi_i\delta\phi_{k,x} + \phi_{k,x}\delta\phi_i)] \Big)dx = 0 \qquad W^0_j = C_{jj}\phi^0_{j,xx} \quad , \quad (3)$$

where (i) C_{ik}, D^1_{ik}, D^2_{ik} and B_{ik} are second-order tensors providing the member linear stiffness, (ii) $f_{R.ik}$ and $F_{P.ik}$ are the generalized forces associated with the continuous and discrete translational and rotational springs, (iii) λ is the load parameter and (iv) $X^{\sigma-x}_{jik}$ and X^τ_{jik} are the geometric stiffness tensors stemming from the pre-buckling longitudinal normal stresses σ^0_{xx} (W^0_1, W^0_2, W^0_3 and W^0_4 concern the compressive axial force, major/minor axis bending moment and bi-moment) and shear stresses τ^0_{xs} (minor/major axis shear and bi-shear associated with the major/minor axis bending moment and bi-moment gradients). The components of these tensors and vectors are given by (E, υ and G are the material Young's modulus, Poisson's ratio and shear modulus)

$$C_{ik} = E\int_b t\,u_i u_k ds + \frac{E}{12(1-\upsilon^2)}\int_b t^3\, w_i w_k ds \qquad B_{ik} = \frac{E}{12(1-\upsilon^2)}\int_b t^3\, w_{i,ss} w_{k,ss} ds$$

$$D^1_{ik} = \frac{G}{3}\int_b t^3\, w_{i,s} w_{k,s} ds \qquad D^2_{ik} = \frac{\upsilon E}{12(1-\upsilon^2)}\int_b t^3\, w_i w_{k,ss} ds \quad , \quad (4)$$

$$X^{\sigma-x}_{jik} = \frac{E}{C_{jj}}\int_b t\,u_j(v_i v_k + w_i w_k) ds \qquad X^\tau_{jik} = \frac{E}{C_{jj}}\int_b H_j(s) w_{i,s} w_k ds \quad , \quad (5)$$

$$f_{R,ik} = \kappa_y v_i(s_R) v_k(s_R) \qquad f_{R,ik} = \kappa_\theta w_{i,s}(s_R) w_{k,s}(s_R)$$

$$F_{P,ik} = K_y v_i(s_P) v_k(s_P) \qquad F_{P,ik} = K_\theta w_{i,s}(s_P) w_{k,s}(s_P) \quad , \quad (6)$$

where (i) $H_j(s)$ is the first moment of (i_1) a cross-section zone, with respect to the major/minor axis ($j=2$ or 3), or of (i_2) a sectorial area zone, with respect to the shear centre ($j=4$) and (ii) $v_j(x_P, s_P)$ and $w_{j,s}(x_P, s_P)$ are the transverse displacement and flexural rotation at P due to deformation mode j.

2.2 Finite element implementation

In order to be able to carry out the purlin buckling (bifurcation) analysis, a GBT-based finite element was implemented. This was achieved by approximating the modal amplitude functions $\phi_k(x)$ using standard Hermite cubic polynomials,

$$\phi_k(x) = d^e_{k.1}\Psi_1(\xi) + d^e_{k.2}\Psi_2(\xi) + d^e_{k.3}\Psi_3(\xi) + d^e_{4.1}\Psi_4(\xi) \quad , \quad (7)$$

where (i) $d^e_{k.1} = \phi_{k,x}(0)$, $d^e_{k.2} = \phi_k(0)$, $d^e_{k.3} = \phi_{k,x}(L_e)$, $d^e_{k.4} = \phi_k(L_e)$, (ii) $\xi = x/L_e$, L_e is the finite element length and (iii) one has

$$\Psi_1 = L_e(\xi^3 - 2\xi^2 + \xi) \qquad \Psi_2 = 2\xi^3 - 3\xi^2 + 1 \qquad \Psi_3 = L_e(\xi^3 - \xi^2) \qquad \Psi_4 = -2\xi^3 + 3\xi^2 \quad . \quad (8)$$

Introducing (7)-(8) into (3) and carrying out the integrations over L_e, one obtains the finite element linear stiffness matrix $[K^e]$ and geometric stiffness matrix $[G^e]$, which are given by

$$K^{ik}_{pr} = C_{ik}\int_{L_e}\Psi_{p,xx}\Psi_{r,xx}d\xi + D_{ik}\int_{L_e}\Psi_{p,x}\Psi_{r,x}d\xi + B_{ik}\int_{L_e}\Psi_p\Psi_r d\xi$$
$$+ f^y_{R.ik}\int_{L_e}\Psi_p\Psi_r d\xi + f^\theta_{R.ik}\int_{L_e}\Psi_p\Psi_r d\xi + \sum_{P=1}^{m}F^y_{P.ik}\Psi_p(x_P)\Psi_r(x_P) + \sum_{P=1}^{m}F^\theta_{P.ik}\Psi_p(x_P)\Psi_r(x_P) \quad , \quad (9)$$

$$G^{ik}_{pr} = W^0_{lj}X^{\sigma-x}_{ikj}T^l_{pr} - W^0_{lj}(S^l_{rp}X^\tau_{jik} + S^l_{pr}X^\tau_{jki}) \quad , \quad (10)$$

where

$$T^l_{pr} = \int_{L_e}\xi^l\Psi_{p,x}\Psi_{r,x}d\xi \quad (l \geq 0) \qquad S^l_{pr} = \frac{l}{L_e}\int_{L_e}\xi^{l-1}\Psi_{p,x}\Psi_r d\xi \quad (l \geq 1) \quad . \quad (11)$$

and the summation convention applies to subscript l ($l=0,1,2,3$), associated with the order of the W_{lj} term – the T^l_{pr} and S^l_{pr} components incorporate the longitudinal stress gradient and shear stress effects. Finally, one last word to mention that, as it would be logical to expect, the elementary geometric stiffness matrix $[G^e]$ is symmetric, even if its evaluation involves the two asymmetric matrices X^τ_{jik} and S^l_{pr}.

The member buckling equations are then obtained by assembling the finite element matrices, which leads to the eigenvalue problem

$$([K] - \lambda[G])\{d\} = \{0\} \quad , \quad (12)$$

Where (i) λ is the load parameter (all applied stresses depend linearly on λ), (ii) $[K]$ and $[G]$ are the member overall linear and geometrical stiffness matrices and (iii) $\{d\}$ is the generalized modal amplitude vector (its components are the problem unknowns). The buckling (bifurcation) loads are the eigenvalues of (9) and the corresponding buckling mode shapes are the associated eigenvectors.

3. Buckling Behavior of Continuously Restrained Simply Supported Purlins

This section addresses the buckling behavior of simply supported purlins submitted to uplift uniformly distributed loads applied along the shear centre axis, which means that they do not cause torsion (see Fig. 4). In order to simulate the restraints provided by the roof sheeting, continuous translational and rotational elastic springs, with stiffness k_y and k_θ, are continuously (along the whole purlin length) attached to the upper flange mid-points. Two cross-sections are considered, namely lipped channels and zed-sections, and their mid-line dimensions and material properties are given in Fig. 5, which also shows the GBT cross-section discretizations adopted. Each of them leads to *13* deformation modes and Figs. 6(a)-(b) display the in-plane shapes of the eight most relevant ones (for each cross-section): modes **2**-**4** are *global* (major and minor axis bending and torsion – the axial extension mode **1** is not shown), modes **5**-**6** are *distortional* and the remaining three deformation modes (≥**7**) are *local*.

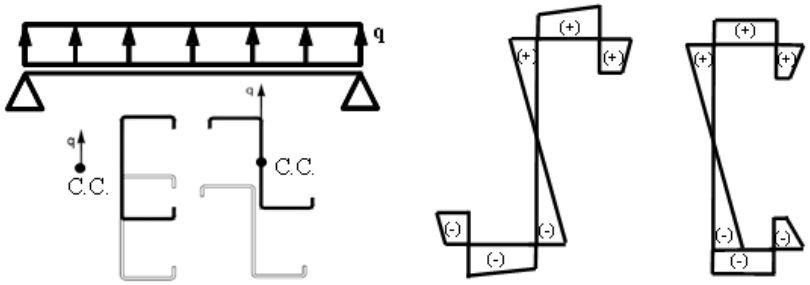

Figure 4: (a) Structural model with the load point of application and (b) pre-buckling normal stress distributions.

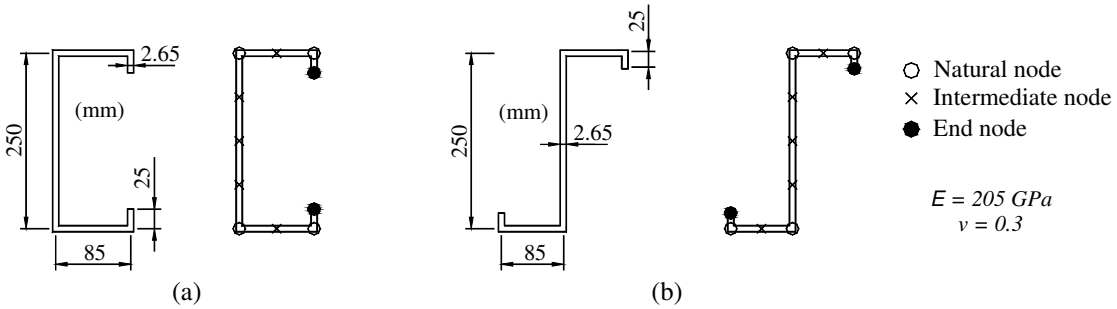

Figure 5: Geometries and GBT discretizations adopted: (a) lipped channel and (b) zed-section.

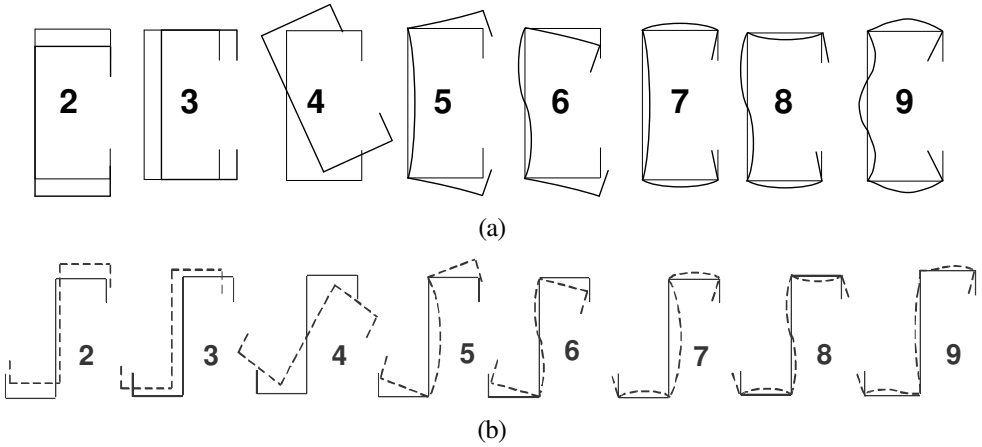

Figure 6: In-plane shapes of the eight most relevant GBT deformation modes: (a) lipped channel and (b) zed section.

Figs. 7(a)-(b) show the variation of the critical buckling moment M_{cr} with the beam span L for the four sheeting restraint conditions corresponding to all possible combination of *continuous* translational and rotational springs with null and infinity stiffness values (k_y and k_θ equal to *0* or ∞). Besides the GBT-based results, obtained with *10* equal-length finite elements (continuous lines), these figures also display, for validation and comparison purposes, some values determined by means of ANSYS shell finite element analyses, adopting fine SHELL63 element meshes (white circles). As for Figs. 8(a)-(b), they show the GBT-based mid-span cross-section buckled shapes concerning the combinations of purlins lengths and restraint conditions indicated in Figs. 7(a) (lipped channels) and 7(b) (zed-sections). Finally, (i) Figs. 9(a)-(d) and 10(a)-(d) provide the GBT modal participation diagrams concerning the critical buckling modes of the lipped channel and zed-section purlins exhibiting the various restraint conditions, and (ii) Figs. 11(a)-(c) show, for $k_y=k_\theta=\infty$ and $L=40,400,800\,cm$, several representations of the purlin critical buckling mode shapes: (i) GBT modal amplitude functions and (ii) ANSYS and GBT 3D views. The close observation of the buckling results displayed in all these figures prompts the following remarks:

(i) The GBT and ANSYS buckling moments virtually coincide (all differences below *3.0%*), despite the huge disparity between the d.o.f. numbers involved in applying each model. For instance, for

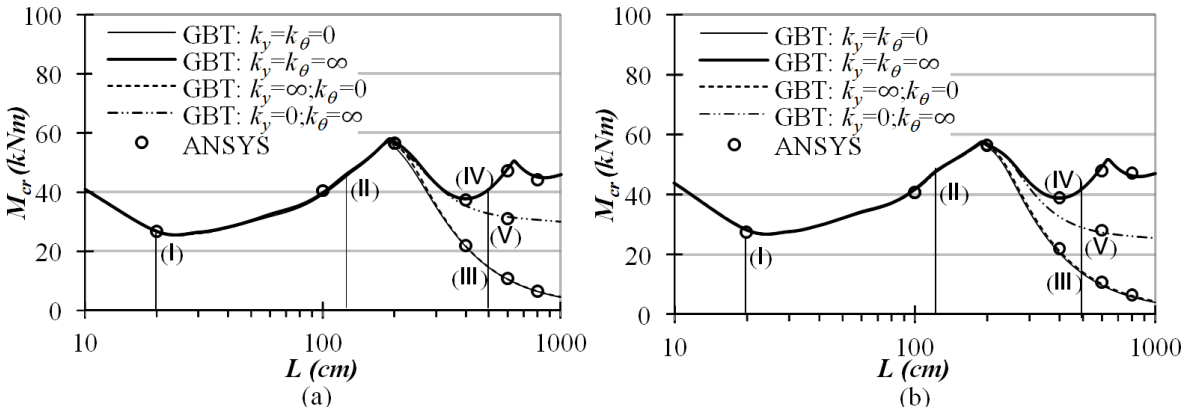

Figure 7: Variation of the critical buckling moment M_{cr} with L: (a) lipped channel and (b) zed-section purlins.

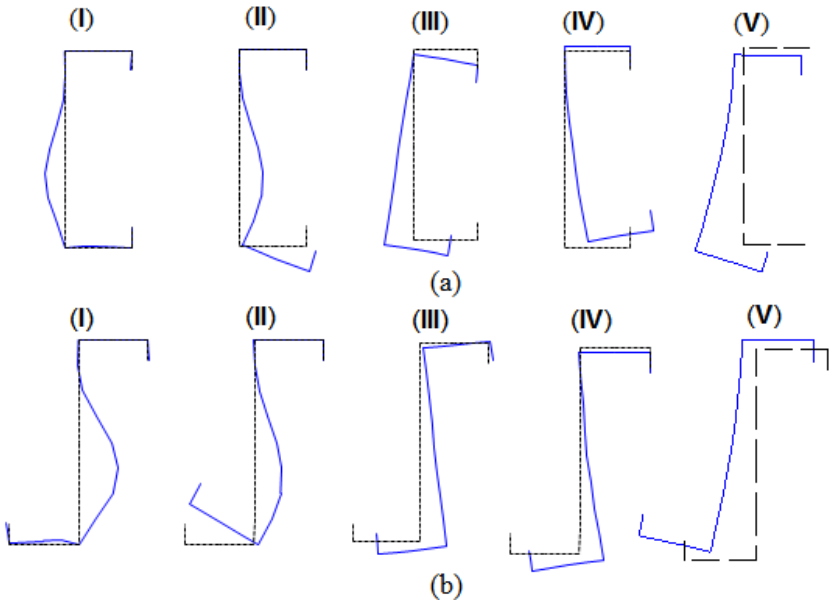

Figure 8: Variation with L of the (a) lipped channel and (b) zed-section purlin mid-span cross-section buckled shape.

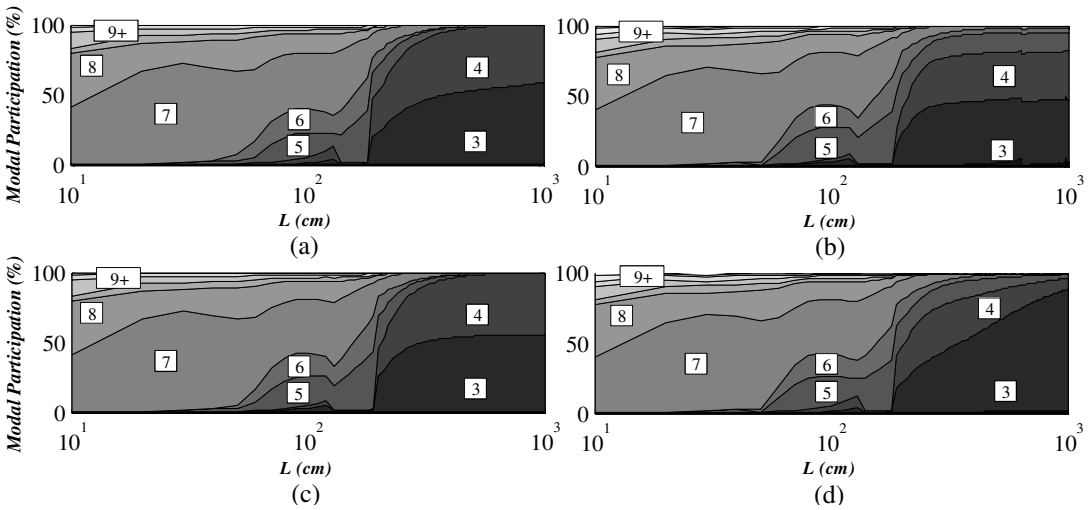

Figure 9: GBT modal participation diagrams of the lipped channel purlin critical buckling modes: (a) $k_y=k_\theta=0$, (b) $k_y=k_\theta=\infty$; (c) $k_y=\infty + k_\theta=0$ and (d) $k_y=0 + k_\theta=\infty$.

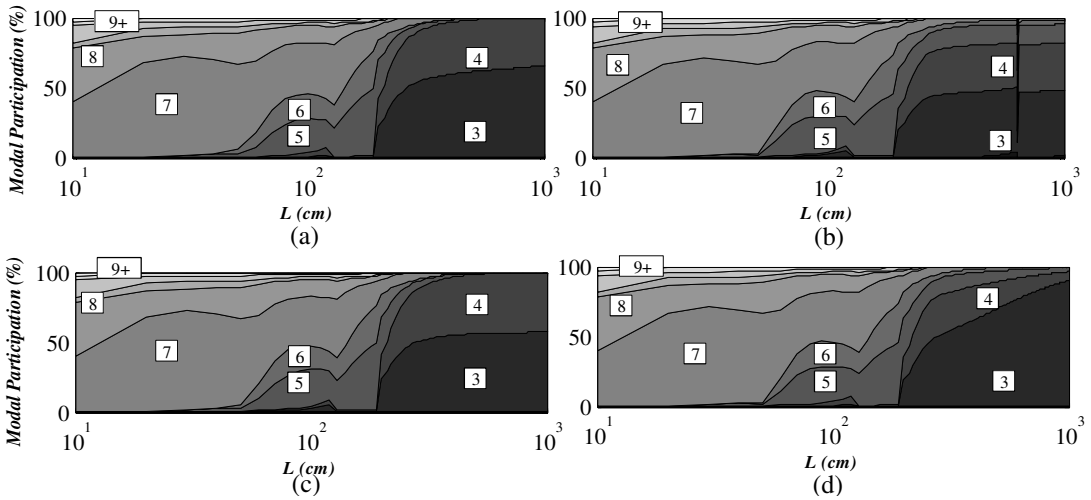

Figure 10: GBT modal participation diagrams of the zed-section purlin critical buckling modes: (a) $k_y=k_\theta=0$, (b) $k_y=k_\theta=\infty$, (c) $k_y=\infty + k_\theta=0$ and (d) $k_y=0 + k_\theta=\infty$.

L=800cm the GBT results were obtained with *360* d.o.f. (*10* equal-length beam finite elements), while the ANSYS ones required considering about *16000* d.o.f. (*i.e.*, about *45* times more).

(ii) The comparison between the various figures clearly shows that the critical buckling behaviors of the lipped channel and zed-section purlins are extremely similar (practically identical). Therefore, unless otherwise specifically mentioned, the comments and remarks included in the next items apply to both the lipped channel and zed-section purlin buckling results.

(iii) For $L \leq 200cm$, the buckling behavior is independent from the restraint conditions – note that the four buckling curves plotted in Figs. 7(a)-(b) are practically coincident. This is due to the fact that the critical buckling modes, combining participations from local and/or distortional modes, do not involve upper flange horizontal displacements or rotations – see the buckled shapes (**I**) and (**II**) in Figs. 8(a)-(b). Moreover, it is worth noting that, within this length range, the critical moment values are strongly influenced by shear buckling, as shown by Bebiano *et al.* (2007) and illustrated in Fig. 11(a), concerning *L=40cm* – note the typical inclined shear buckles near the end supports.

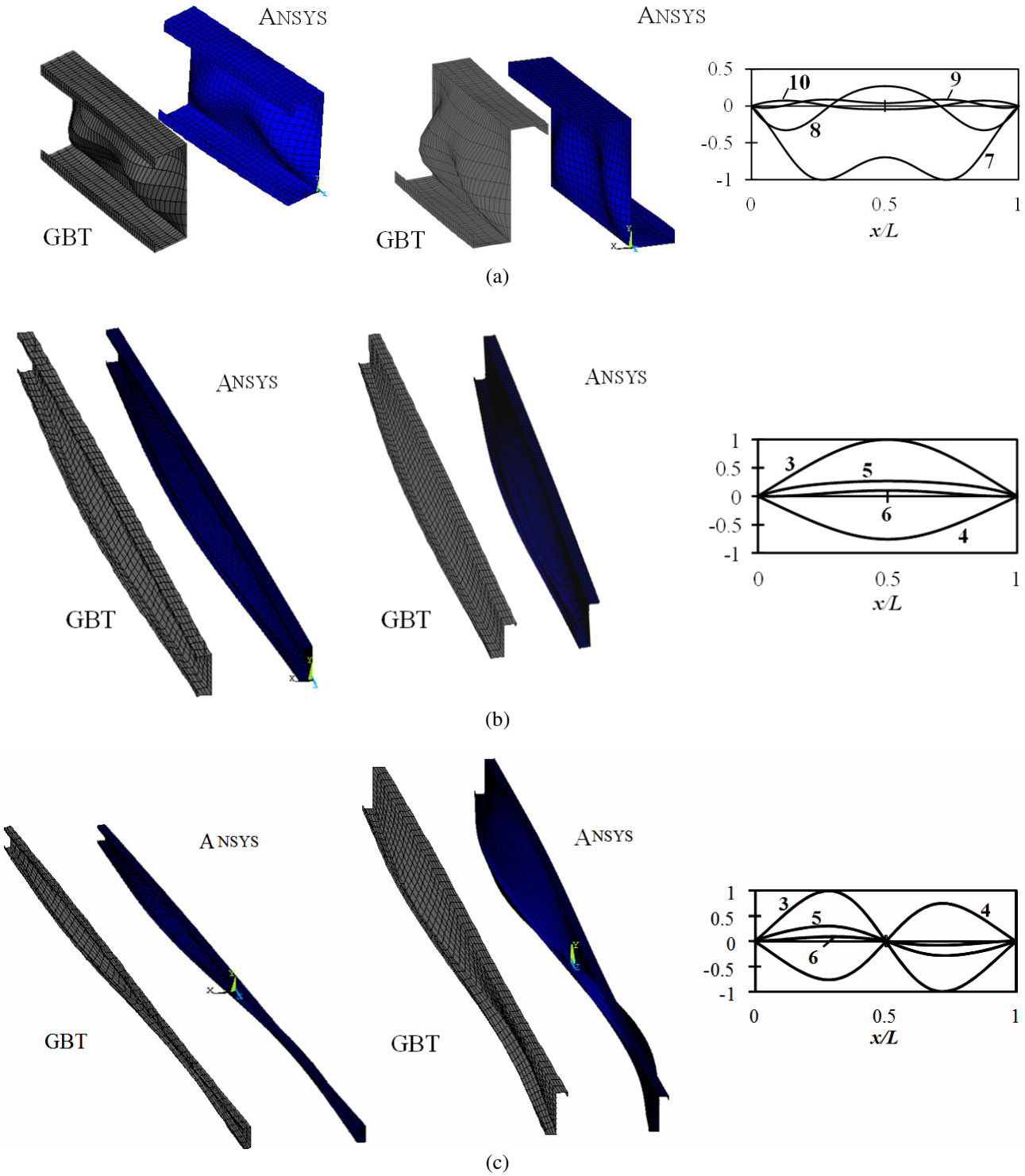

Figure 11: GBT and ANSYS 3D views and GBT modal amplitude functions concerning the critical buckling mode shapes of lipped channel and zed-section purlins with $k_y=k_\theta=\infty$ and (a) *L=40 cm*, (b) *L=400 cm* and (c) *L=800 cm*.

(iv) For *L>200 cm*, Figs. 9(a)-(d) and 10(a)-(d) reveal the sudden emergence and subsequent dominance of the global modes **3** (minor axis bending) and **4** (torsion), which logically entails a strong influence of the sheeting restraint on the purlin buckling behavior, clearly visible in Figs. 7(a)-(b).

(v) In the unrestrained purlins ($k_y=k_\theta=0$), flexural-torsional buckling occurs and a very pronounced M_{cr} drop takes place. The buckled shapes (**III**) in Figs. 8(a)-(b) show that the horizontal displacement of the point of translational restraint is minute, making it logical to anticipate that the influence of k_y will be negligible. This assertion is confirmed by the almost coincidence between the buckling curves associated with $k_y=k_\theta=0$ and $k_y=\infty + k_\theta=0$. However, it is worth noting that this minute horizontal displacement is slightly larger for the zed-section purlins, which provides the explanation for the (barely) perceptible differences between the two above buckling curves – with the adopted scale, there is literally no difference between their lipped channel counterparts. It will be shown in section 4 that this behavioral difference separating the lipped channel and zed-section buckling behaviors has some impact on the effects due to the translational spring (finite) stiffness.

(vi) For $k_y=0 + k_\theta=\infty$, the M_{cr} vs. L curve is qualitatively similar to that concerning $k_y=k_\theta=0$, but naturally corresponds to higher critical buckling moments due to the added rotational stiffness. On the other hand, the modal participation diagrams shown in Figs. 9(d) and 10(d) show that the rotational restraint leads to a decrease in the participation of mode **4** (torsion), which is "compensated" by the increased contributions of mode **3** (minor axis bending) and, mostly, mode **5** (symmetric distortion) – these contributions, required to suppress the upper flange rotation, increase with the purlin length L. The buckled shapes (**V**) in Figs. 8(a)-(b) illustrate the buckling modes of these restrained purlins, which are characterized by the occurrence of (vi_1) horizontal displacements of the upper flange, due to mode **3**, and (iv_2) lower flange distortion, due to mode **5** – this deformation mode participation is responsible for the designation *lateral-distortional buckling*.

(vii) For $k_y=k_\theta=\infty$, the previous horizontal displacements (due to $k_\theta=\infty$, *i.e.*, occurring for $k_y=0 + k_\theta=\infty$) are fully restrained, thus causing a significant M_{cr} increase (the purlin stiffness is higher) stems from the lower participation of deformation mode **3**, compensated by larger contributions from modes **4** and **5**. The buckled shapes (**IV**) in Figs. 8(a)-(b) provide clear evidence of the occurrence of a lateral-distortional buckling mode that does not involve upper flange horizontal displacements – this instability phenomenon was investigated and reported by Hancock *et al.* (2001). In order to assess the quantitative benefits associated with restraining the upper flange horizontal displacements (in addition to restraining its torsional rotations), consider the lipped channel purlins with *L=400 cm* and *L=600 cm*: M_{cr} increases by (vii_1) *75.6%* and *345.5%*, with respect to $k_y=k_\theta=0$, and by (vii_2) *72.4%* and *181.8%*, with respect to $k_y=0 + k_\theta=\infty$.

(viii) The M_{cr} vs. L curve for $k_y=k_\theta=\infty$ exhibits two distinct branches associated with lateral-distortional buckling, concerning single and two half-wave lower flange distortional deformations. This can be clearly visualized by observing the ($viii_1$) critical buckling modes shapes and ($viii_2$) mode **5** and **6** amplitude functions of the *L=400 cm* and *L=800 cm* purlins, which are shown in Figs. 11(b)-(c).

(ix) It is worth noting that the influence of k_y is completely different for k_θ=0 and $k_\theta=\infty$: quite strong in the second case and practically non-existent in the first one – the translational spring is "activated" only if the upper flange rotations are restrained (this triggers the emergence of horizontal displacements).

(x) Finally, attention is called to the fact that the M_{cr} value depends on the purlin span L (indeed, it is proportional to $q_{cr}L^2$). This explains why the M_{cr} vs. L curve does not descend monotonically within the whole span range – this would obviously be the case for a q_{cr} vs. L curve.

4. Influence of the Translational/Rotational Restraint Stiffness on the Purlin Buckling Behavior

This section addresses the influence of the amount of translational and/or rotational restraint stiffness, provided by the roof sheeting, on the buckling behaviors of the simply supported lipped channel and zed-

section purlins. The numerical results presented and discussed concern purlins with two different lengths, namely $L=400,600\,cm$, and discretely restrained against the upper flange horizontal (in-plane) translations and rotations. The restraints are modeled by means of equally spaced elastic supports (i) with stiffness values K_y (translation) K_θ (torsion) and (ii) located at $a=40\,cm$ intervals, corresponding to the distance between adjacent self-drilling screws. The above numerical results consist of critical moments obtained through GBT beam finite element and ANSYS shell finite element analyses – while the former involved *360* or *540* d.o.f. ($L=400\,cm$ or $L=600\,cm$ – *10* or *15* equal-length beam finite elements), the latter required around *12000* or *14000* d.o.f. (*i.e.*, now about *30* times more – recall that this ratio was *45* in section 3).

Figs. 12(a)-(b) show the variations of M_{cr} with K_θ, for the four combinations between $L=400,600\,cm$ and $K_y=0,\infty$. As for Fig. 12(c), it concerns the restraint condition defined by $K_y=0$ + $K_\theta=\infty$ and depicts the longitudinal profiles of the upper flange mid-point (the point of translational restraint, if $K_y\neq 0$) horizontal displacements – $\delta=\delta(x/L)$. Then, Figs. 12(d)-(e) display the variation of M_{cr} with K_y, again for $L=400,600\,cm$ but now only for $K_\theta=\infty$, making it possible to identify the minimum translational restraint stiffness required to "virtually preclude" the occurrence of upper flange horizontal displacements (for $K_\theta=\infty$). Finally, Figs. 13(a)-(b) compare the (i) mode **3**, **4** and **5** amplitude functions and (ii) mid-span cross-section deformed configurations, for $L=600\,cm$ and $K_y=K_\theta=0$ or $K_y=0$ + $K_\theta=5\,kNm/rad$ – note that the modal amplitude functions are practically the same for the lipped channel and zed-section purlins. The analysis of all these buckling results makes it possible to draw the following conclusions:

(i) As before, there is an excellent correlation between the M_{cr} values provided by the GBT and ANSYS buckling analyses – indeed, the differences never exceed *5.0%*.

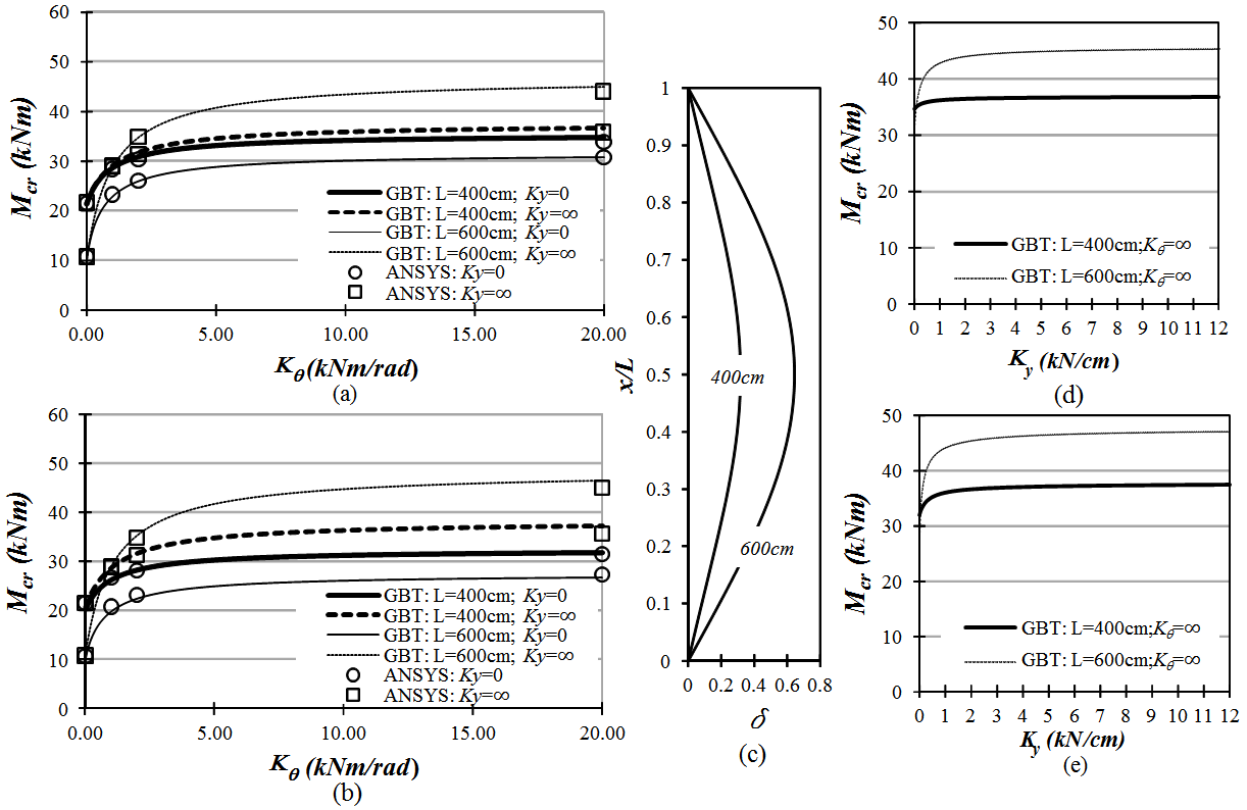

Figure 12: (a) Lipped channel and (b) zed-section purlin M_{cr} vs. K_θ curves, (c) critical buckling mode upper flange horizontal displacements for $K_y=0$ + $K_\theta=\infty$, and (d) lipped channel and (e) zed-section purlin M_{cr} vs. K_y curves.

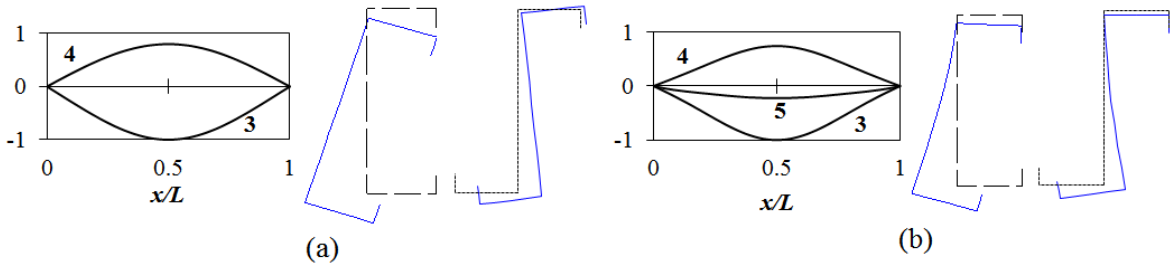

Figure 13: GBT critical buckling mode modal amplitude functions and mid-span cross-section buckled shapes concerning lipped channel and zed-section purlins with $L=600\ cm$ and (a) $K_y=K_\theta=0$ or (b) $K_y=0+K_\theta=5\ kNm/rad$.

(ii) As it would be logical to expect, M_{cr} increases with K_θ for all the eight purlins considered here. The M_{cr} vs. K_θ curve exhibits an initial (small K_θ values) portion that is rather steep (larger slopes for $L=600\,cm$), followed by a smooth asymptotic increase towards the value associated with $K_\theta=\infty$. Due to the high initial slopes, $M_{cr}(\infty)$ is always considerably above $M_{cr}(0)$ – the difference is more relevant for $L=600\,cm$ than for $L=400\,cm$, for cumulative reasons (higher $M_{cr}(\infty)$ and lower $M_{cr}(0)$).

(iii) The M_{cr} increase stems from the fact that the nature of the critical buckling mode changes. Figs. 13(a)-(b) shows the mid-span cross-section buckled shapes concerning $L=600\,cm$, $K_y=0$ and $K_\theta=0$ or $K_\theta=5\,kNm/rad$. It is worth noting that the emergence of mode **5** (symmetric distortion) cancels the flange rotation due to mode **4**, thus leading to the occurrence of lateral-distortional buckling.

(iv) For the two lengths considered, the amount of rotational stiffness required to "almost fully restrain" the purlins is fairly low. Adopting the criterion $M_{cr}\geq 0.95M_{cr}(\infty)$ to ensure a "fully restrained" purlin, one has $(K_\theta)_{min}=5\,kNm/rad$, for $L=400\,cm$, and $(K_\theta)_{min}=8\,kNm/rad$, for $L=600\,cm$ (in both purlins).

(v) Logically, M_{cr} also increases with K_y for the four purlins analyzed (only with $K_\theta=\infty$). The M_{cr} vs. K_y curves, which are qualitatively similar to their M_{cr} vs. K_θ counterparts, show that the influence of K_y is much more pronounced for $L=600\,cm$ than for $L=400\,cm$ – the $M_{cr}(\infty)/M_{cr}(0)$ ratios are equal to *1.33* and *1.05*, respectively. On the other hand, adopting the criterion $M_{cr}\geq 0.99M_{cr}(\infty)$ to ensure a "fully restrained" purlin, one has $(K_y)_{min}=1\,kN/cm$ (lipped channel) or $(K_y)_{min}=2\,kN/cm$ (zed-section), for $L=400\,cm$, and $(K_y)_{min}=8\,kN/cm$ (lipped channel and zed.section), for $L=600\,cm$.

(vi) There are no significant differences between the M_{cr} values obtained for purlins restrained by continuous and "equivalent" (with the same "overall resultant") discrete restraints. For instance, for $K_y=K_\theta=\infty$, M_{cr} is about *4%* lower in the case of equally spaced discrete restraints (a=*40 cm*), for either $L=400\,cm$ and $L=600\,cm$. Therefore, the consideration of continuous restraints, far simpler to model that their discrete counterparts, provides fairly acceptable purlin critical buckling results.

(vii) Finally, it is worth noting that the M_{cr} increase with K_θ is more pronounced for $K_y=\infty$. As mentioned earlier, this fact stems from the occurrence of non-negligible upper flange horizontal displacements for $K_y=0$ – they are shown in Fig. 12(c), where the larger values for $L=600\,cm$ are clearly visible (recall that these displacements are practically if, in addition, one has $K_\theta=0$). This means that the absence of horizontal displacements increases the rotational restraint efficiency. Moreover, note that this effect is more relevant in the zed-section purlins, which is due to the fact that the vertical loading causes pre-buckling biaxial bending (see Fig. 4(b)).

4.1 Rotational Stiffness Assessment

In order to illustrate the assessment of the ability of commonly used steel roof sheets to provide adequate rotational restraint to purlin upper flanges, a numerical example is presented next. It concerns the evaluation of the rotational stiffness of a slender (*Class 4*, in the Eurocode 3 EN1993-1-3 nomenclature –

CEN 2005) trapezoidal steel sheet ($E=205\,GPa$ and $\nu=0.3$) exhibiting the geometry depicted in Fig. 14. This evaluation was made according to the methodology prescribed in clause 10.1.5.2 of EN1993-1-3 (CEN 2006), taking into account both the (i) steel sheet bending flexural stiffness and (ii) purlin-sheet connection stiffness, associated in series. The numerical results obtained are based on (i) the purlin cross-section dimensions given in Fig. 5, (ii) a distance $s=200\,cm$ between adjacent purlins and (iii) a spacing $a=40\,cm$ between consecutive self-drilling screws. They consist of (i) $C_{D.C}=88.3\,kNm/rad$ (rotational stiffness stemming from the steel sheet bending), (ii) $C_{D.A}=5.3\,kNm/rad$ (rotational stiffness provided by the connection between the steel sheet and purlin) and (iii) $K_\theta=5.0\,kNm/rad$ (overall rotational stiffness, combining the two above contributions). It is worth noting that:

(i) The rotational stiffness stemming from the trapezoidal steel sheet bending is about *17* times higher than that of its purlin-sheet connection counterpart: $88.3\,kNm/rad$ vs. $5.3\,kNm/rad$. Since the two stiffening contributions are associated in series, the overall rotational stiffness is just a tiny fraction below the value due to the purlin-sheet connection: $5.0\,kNm/rad$.

(ii) The calculated overall rotational stiffness ($K_\theta=5.0\,kNm/rad$) (ii_1) virtually coincides with the $(K_\theta)_{min}$ value obtained for $L=400\,cm$ and (ii_2) falls quite below its $L=600\,cm$ counterpart: $(K_\theta)_{min}=8\,kNm/rad$.

(iii) In view of the above values, it is readily concluded that the sizeable beneficial effect stemming from the rotational stiffness provided by the whole roof sheeting system should be taken into account when calculating the purlin critical buckling moment M_{cr}. In this particular case, for $L=400\,cm$, the stiffness value provided even ensures "full rotational restraint".

(iv) Since the overall rotational stiffness is governed by the purlin-sheet connection flexibility, its increase has a strong impact on the purlin critical buckling behavior. One straightforward way of achieving a higher $C_{D.A}$ value (and, therefore, also a higher K_θ value) is to adopt purlins with wider flanges.

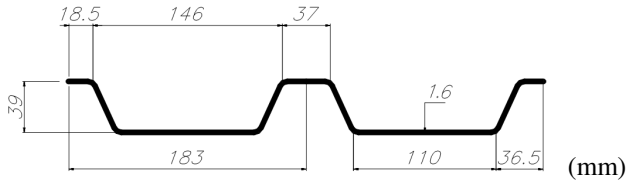

Figure 14: Illustrative example: trapezoidal steel sheet geometry.

5. Continuous Purlins – Strengthening of Intermediate Support Regions

In practice, many cold-formed steel purlins exhibit multiple spans and are subjected to non-uniform bending moment diagrams combining positive (sagging) and negative (hogging) regions. This fact makes their buckling behavior rather complex, as it may (i) combine local, distortional and global features and (ii) involve a fair amount of localization (*e.g.*, the occurrence of local and/or distortional buckling in the vicinity of intermediate supports, where relevant moment gradients occur and little restraint can be offered to the slender bottom/compressed flanges). Even so, it seems fair to say that the amount of research devoted to the structural behavior of cold-formed steel purlins under non-uniform bending is still relatively scarce. In this context, it is worth noting the recent works of (i) Pham & Hancock (2009), who proposed a design criterion based on the Direct Strength Method (DSM) for purlin-sheeting systems, (ii) Zhang & Tong (2008) and Dubina & Ungureanu (2010), who studied the structural behavior of lapped connections over the intermediate supports in multi-span cold-formed steel zed-section purlin systems.

One possible way of improving the continuous purlin resistance against local or distortional buckling and/or failure in the vicinity of intermediate supports consists of strengthening that region. This can be

done by means of several procedures that basically amount to doubling the purlin wall thickness along the strengthened length. Fig. 15 illustrates one of those procedures, which is employed when the purlin is continuous over the intermediate support: a plain channel "sleeve" is bolted around the lipped channel purlin along the strengthening length – both the purlin and "sleeve" share the same wall thickness. Alternative procedures, unavoidable in purlins connected at an intermediate support location, consist of (i) adopting a bolted "sleeve" to "cover" the joint (lapped joint) or (ii) joining/bolting the connected purlins along a finite length centred at the intermediate support (overlap joints) – the two purlins can be joined internally ("one inside the other") or externally ("one next to the other"). However, in all cases it is not clear which is the "optimal strengthening/lap/overlap length", *i.e.*, the minimum length that needs to be strengthened in order to preclude the occurrence of local or distortional buckling and/or failure.

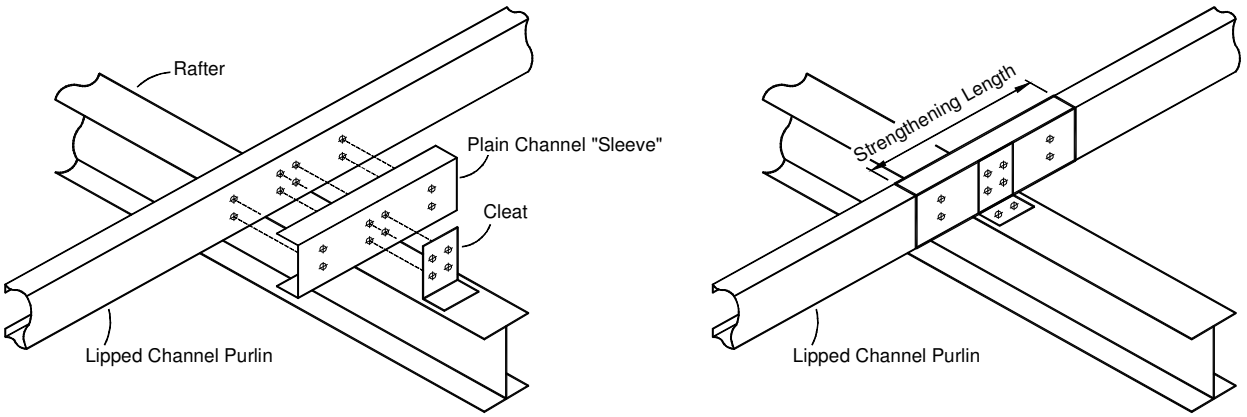

Figure 15: Detail of the "sleeve" strengthening of a continuous lipped channel purlin intermediate support region.

A GBT-based strategy to estimate the optimal (minimum) strengthening/lap/overlap length in continuous purlins is proposed and illustrated in this work. It involves the performance of a GBT buckling analysis of the un-strengthened purlin, in order to identify the length of the intermediate support region where significant local and/or distortional deformation occurs – the criterion adopted consists of taking the length between the left and right most deformed (locally and/or distortionally) cross-sections, which can be easily identified from the observation of the GBT modal amplitude functions.

The illustrative example presented and discussed concerns the cold-formed steel lipped channel two-span purlin depicted in Fig. 16(b), with length $L=8.0\,m$ and the cross-section dimensions and material properties given in Fig. 16(a). The purlin (i) is acted by a uniformly distributed gravity load applied along the shear centre longitudinal axis, which causes only pre-buckling major-axis bending (diagram shown in Fig. 16(b)), (ii) has end sections locally/globally pinned and able to warp freely, and (iii) rests on an

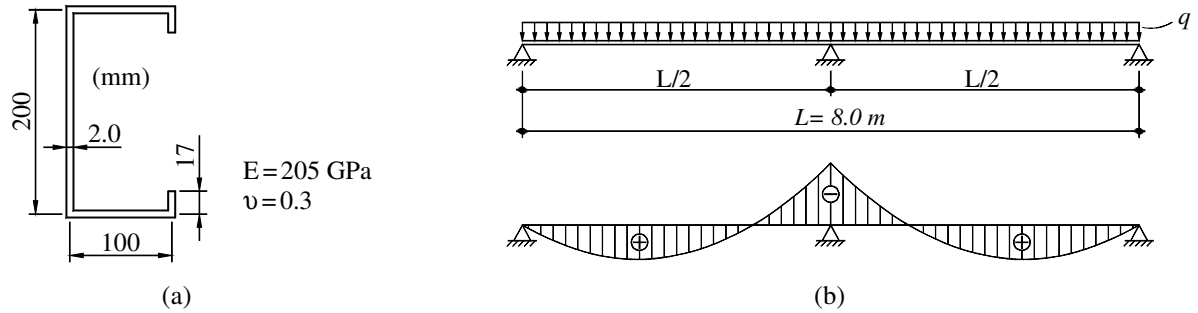

Figure 16: Two-span purlin (a) cross-section dimensions and (b) loading and 1st-order elastic bending moment diagram.

intermediate support that restrains all the in-plane cross-section displacements. Moreover, it is assumed that the purlin continuity over the intermediate support in ensured by an overlap joint, which means that doubling the wall thickness along the strengthened length provides an adequate structural model. Finally, one last word to mention that the restraints provided by the roof sheeting are not considered in this study – *i.e.*, the purlin is analyzed with an unrestrained upper flange.

Fig. 17(a) displays the GBT modal amplitude functions concerning the critical buckling mode of the behavior of the un-strengthened two-span purlin. On the other hand, Fig 17(b) provides ANSYS 3D views of the same critical buckling mode shape, obtained by discretizing the purlin into a fine SHELL181 finite element mesh. At the outset, note that the GBT and ANSYS critical buckling (uniformly distributed) loads virtually coincide: $q_{cr.GBT}=10.82\,kN/m$ and $q_{cr.ANSYS}=10.71\,kN/m$ (*1.03%* difference). Then, the observation of the two buckling mode representations given in Figs. 17(a)-(b) prompts the following remarks:

(i) The GBT and ANSYS buckling mode representations are in a very close agreement – this fact is particularly striking around the intermediate support (see the zoomed detail in Fig. 17(b)).

(ii) The purlin buckling action involves mostly the more or less close vicinity of the intermediate support – Fig. 17(a) shows that there are (ii_1) major contributions from the distortional modes **5**-**6** and also (ii_2) non-negligible ones from the local modes **7**-**8** (note that such a detailed structural identification cannot be obtained from the output of the ANSYS shell finite element analysis).

(iii) Fig. 17(a) clearly shows that the distortional deformations (modes **5** and **6** amplitude functions) exhibit maximum values at cross-sections located about *270mm* to the left and to the right of the intermediate support.

(iv) Since the mode **5** and **6** amplitude functions have the same sign, the bottom/compressed flange rotations caused by theses two deformation modes are additive (see Fig. 6(a)), which explains the very pronounced rotation of this flange in the intermediate support region – see Fig. 17(b).

(v) The global modes **3** and **4** (minor-axis bending and torsion) play a lesser role – their contributions are only meaningful well inside the purlin spans, *i.e.*, quite far away from the intermediate support.

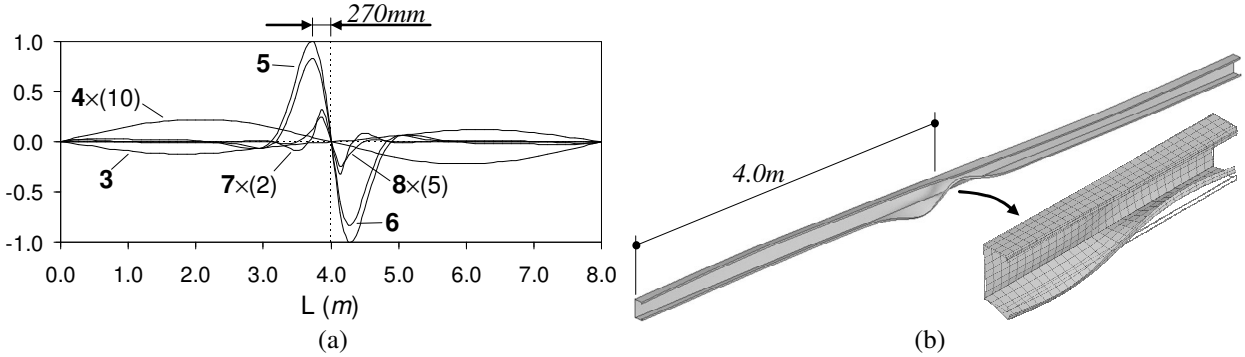

Figure 17: (a) GBT and (b) ANSYS representations of the un-strengthened purlin buckling mode shape

Following the GBT-based strategy devised, purlin strengthening consists of considering an overlap length equal to *540mm*, corresponding to the region (centered on the intermediate support) exhibiting the most locally and/or distortionally buckled configuration. This would be the optimal (minimum) overlap length, in the sense that it involves the highest ratio between the critical buckling load increase and the amount of added material. In order check the validity of this assertion, the next step consists of analyzing the buckling behavior of a purlin strengthened by an overlap length of *540mm*. Figs. 18(a)-(b) show the GBT and ANSYS representations of the strengthened critical buckling mode, which corresponds to

buckling loads $q_{cr.GBT}=15.17kN/m$ and $q_{cr.ANSYS}=15.15kN/m$ (now a *0.13%* difference) – in both analyses the influence of the overlap length was modeled by doubling the purlin wall thickness. After observing these novel buckling results one readily concludes that:

(i) The strengthening procedure led to a very considerable critical buckling load increase: *40.2%*.

(ii) Concerning the critical buckling mode shape, the overlap length has the net effect of significantly altering its nature and characteristics. Indeed, it is evident that (ii_1) the purlin overlap region remains practically unbuckled and (ii_2) the purlin critical buckling is triggered by a combination of distortional (modes **5** and **6**) and global (modes **3** and **4**) deformations, both occurring mostly far away from the intermediate support (their maximum values take place in the mid-span regions) – note the substantial increase of the global deformation contribution. Moreover, there are also lesser participations from the local modes **7** and **8**.

(iii) Although no real optimization study was carried out, it seems logical to expect that an overlap length of *540mm* is not very far from the "optimal length" to strengthen the two-span purlin against the occurrence of local and/or distortional deformations in the vicinity of the intermediate support.

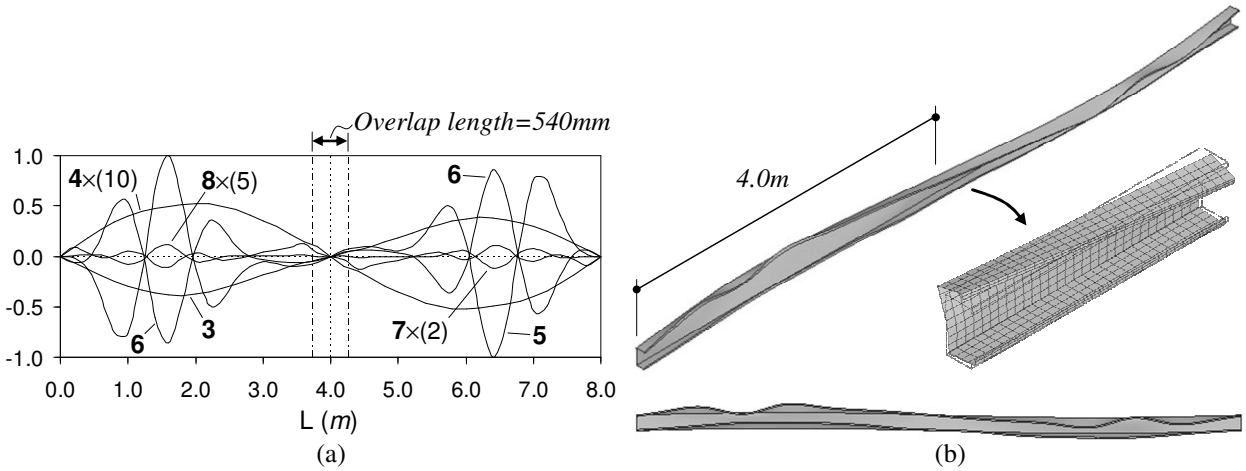

Figure 18: (a) GBT and (b) ANSYS representations of the strengthened (overlapped) purlin buckling mode shape

6. Concluding Remarks

This work presented and discussed the results of a GBT-based numerical investigation concerning the local, distortional and global buckling behavior of simply supported lipped channel and zed-section cold-formed steel purlins restrained by steel sheeting and subjected to a uniformly distributed uplift load. After providing the main concepts and procedures involved in the development of a GBT buckling formulation specifically aimed at the problems under scrutiny, the investigation began by considering purlins continuously restrained against the upper flange horizontal (in-plane) displacements/translations and torsional rotations. For various restraint stiffness combinations, it was determined how the critical buckling moment and mode shape vary with the purlin length – a relevant finding consisted of the fact that the translational restraint can only be meaningfully mobilized if a significant torsional restraint is also present. Next, the focus shifted to discretely restrained purlins with two typical lengths and the GBT analyses were employed to quantify the minimum translational and rotational stiffness values that are required to ensure an "almost full upper flange restraint". Moreover, it was also shown that the minimum rotational stiffness can be fairly easily attained with commonly used trapezoidal steel sheeting, attached to the purlin upper flange by means of self-drilling screws.

Then, the paper closed with a study on the strengthening of a two-span lipped channel purlin, subjected to a uniformly distributed gravity load, against the occurrence of local and/or distortional deformations in the vicinity of the intermediate support, due to the high hogging bending moments. A GBT-based strategy to estimate the optimal/minimum strengthening/lap/overlap length was devised and illustrated. Its application to the above purlin was proven very effective in identifying/determining an optimal/minimum overlap length ensuring that the purlin critical buckling is not triggered close to the intermediate support.

Finally, its is worth noting that several GBT-based results were compared with values yielded by ANSYS shell finite element analyses – the virtually perfect agreement found, both in terms of critical buckling moments/loads and mode shapes, provided adequate validation of the developed GBT formulation.

Acknowledgments

The authors gratefully acknowledge the financial support of "*Fundação para a Ciência e Tecnologia*" (FCT – Portugal), through the research project "Generalised Beam Theory (GBT) – Development, Application and Dissemination" (PTDC/ECM/108146/2008)project. Moreover, the second author is also indebted to FCT for having granted him the post-doctoral scholarship nº SFRH/BPD/62904/2009.

References

Bebiano R, Silvestre N, Camotim D (2007). "GBT formulation to analyze the buckling behaviour of thin-walled members under non-uniform bending", *International Journal of Structural Stability and Dynamics*, **7**(1), 23-54.

Camotim D, Silvestre N, Gonçalves R, Dinis PB (2004). "GBT analysis of thin-walled members: new formulations and applications", *Thin-Walled Structures: Recent Advances and Future Trends in Thin-Walled Structures Technology*, J. Loughlan (ed.), Canopus Publishing Ltd., Bath, 137-168.

Camotim D, Silvestre N, Basaglia C, Bebiano R (2008). "GBT-based buckling analysis of thin-walled members with non-standard support conditions", *Thin-Walled Structures*, **46**(7-9), 800-815.

Camotim D, Basaglia C, Bebiano R, Gonçalves R, Silvestre N (2010b). "Latest developments in the GBT analysis of thin-walled steel structures", *Proceedings of International Colloquium Stability and Ductility of Steel Structures* (SDSS'Rio 2010 – Rio de Janeiro, 8-10/9), E. Batista, P. Vellasco L. de Lima (Eds), 33-58.

Comité Européen de Normalisation (CEN) (2005). *Eurocode 3 – Design of Steel Structures – Part 1-1: General Rules and Rules for Buildings*, EN1993-1-1, Brussels.

Comité Européen de Normalisation (CEN) (2006). *Eurocode 3 – Design of Steel Structures – Part 1-3: General Rules – Supplementary Rules for Cold-Formed Members and Sheeting*, EN1993-1-3, Brussels.

Davies JM (1991). "Sheeting and decking", *Design of Cold-Formed Steel Members*, J. Rhodes (Ed.), Elsevier Applied Science, New York, 339-360.

Davies JM, Leach P, Heinz D (1994). "Second-order generalised beam theory", *Journal of Constructional Steel Research*, **31**(2-3), 221-241.

Dubina D, Ungureanu V (2010). "Behaviour of multi-span cold-formed Z-purlins with bolted lapped connections." *Thin-Walled Structures*, **48**(10-11), 866-871.

Freitas MF (2004). *Screwed Connections in Steel Construction*, M.A.Sc. Dissertation, School of Engineering of São Carlos, University of São Paulo. (Portuguese)

Hancock GJ, Murray TM, Ellifritt DS (2001). *Cold-Formed Steel Structures to the AISI Specification*, Marcel Dekker Inc., New York.

Pham CH, Hancock GJ (2009). "Direct strength design of cold-formed purlins", *Journal of Structural Engineering* (ASCE), **135**(3), 229-238.

SAS (Swanson Analysis Systems Inc.) (2009). *ANSYS Reference Manual* (version 12).

Schardt, R. (1989). *Verallgemeinerte Technische Biegetheorie*, Springer-Verlag, Berlin. (German)

Zhang L, Tong G (2008). "Moment resistance and flexural rigidity of lapped connections in multi-span cold-formed Z purlin systems", *Thin-Walled Structures*, **46**(5), 551-560.